

Article

NiCo₂S₄/MoS₂ Nanocomposites for Long-Life High-Performance Hybrid Supercapacitors

Le Nhu Minh Tue ^{1,†}, Sumanta Sahoo ^{1,†}, Ganesh Dhakal ¹, Van Hoa Nguyen ², Jintae Lee ¹, Yong Rok Lee ¹ and Jae-Jin Shim ^{1,*}

¹ School of Chemical Engineering, Yeungnam University, 280 Daehak-Ro, Gyeongsan 38541, Gyeongsbuk, Republic of Korea

² Department of Chemistry, Nha Trang University, 2 Nguyen Dinh Chieu, Nha Trang, Vietnam

* Correspondence: jjshim@yu.ac.kr; Tel.: +82-53-810-2587

† These authors contributed equally to this work.

Abstract: Metal sulfides (MS) and mixed metal sulfides (MTMS) have been considered potential candidates over their metal oxide/mixed metal oxide counterparts in recent years. Herein, one MTMS, i.e., NiCo₂S₄, was combined with 2D MS MoS₂ through a single-step solvothermal process with different morphologies (sheet-like and rod-like) for supercapacitor applications. The resulting electrode exhibited excellent coulombic efficiency, high specific capacitance, superior energy density, and, most importantly, ultra-high cycling stability. In particular, the electrode delivered a capacitance of 2594 F g⁻¹ at 0.8 A g⁻¹ after 45,000 charge/discharge cycles with a remarkable stability of 192%. Moreover, the corresponding hybrid supercapacitor device displayed an impressive coulombic efficiency of 123% after 20,000 cycles and 118% after 45,000 cycles. In addition, the device also exhibited a decent energy density of 31.9 Wh kg⁻¹ and good cycling stability of 102% over 15,000 cycles.

Keywords: supercapacitor; NiCo₂S₄; MoS₂; coulombic efficiency; cycling stability



Citation: Tue, L.N.M.; Sahoo, S.; Dhakal, G.; Nguyen, V.H.; Lee, J.; Lee, Y.R.; Shim, J.-J. NiCo₂S₄/MoS₂ Nanocomposites for Long-Life High-Performance Hybrid Supercapacitors. *Nanomaterials* **2023**, *13*, 689. <https://doi.org/10.3390/nano13040689>

Academic Editor: Carlos Miguel Costa

Received: 31 December 2022

Revised: 31 January 2023

Accepted: 7 February 2023

Published: 10 February 2023



Copyright: © 2023 by the authors. Licensee MDPI, Basel, Switzerland. This article is an open access article distributed under the terms and conditions of the Creative Commons Attribution (CC BY) license (<https://creativecommons.org/licenses/by/4.0/>).

1. Introduction

Fossil fuel resources are predicted to be depleted in the next few decades. Therefore, developing renewable and clean energy conversion/storage systems will play a key role in fulfilling the future energy demand. Researchers have been exploring innovative synthetic approaches to fabricate advanced energy storage devices for the last few decades. However, it is challenging to explore easy and inexpensive synthesis methods which are industrially viable. Apart from this, economic efficiency is also one of the most critical factors for long-term operation. In this aspect, supercapacitors are considered favorable, clean electrochemical energy storage devices because of their high power density (P_D), high cycle life, and fast charge/discharge ability [1–5].

Supercapacitors can be ordinarily classified into three groups on the basis of their electrochemical storage kinetics: electrical double-layer capacitor (EDLC), pseudocapacitor, and hybrid capacitor (a combination of EDLC and pseudocapacitor). Typically, pseudocapacitor electrodes are fabricated from transition metal oxides and conducting polymers. On the other hand, EDLCs mostly use carbonaceous materials. In general, EDLC exhibits comparatively lower specific capacitance (C_{sp}) and energy density (E_D) than pseudocapacitors because of the fast, reversible redox reactions at the electrode-electrolyte interface of electrodes. However, EDLC has good intrinsic conductivity, chemical stability, P_D , and cycle life. Overall, hybrid capacitors are the best choice for next-generation electronic devices, combining the advantages of both EDLC and pseudocapacitors to produce advanced high-performance supercapacitors [6].

Nevertheless, the E_D of commercialized supercapacitors is still lower than that of batteries and fuel cells, despite being higher than that of conventional dielectric capacitors [7,8]. The E_D can be enhanced by altering several strategies such as improving the

voltage window of the electrolyte, combining the carbon materials with metal oxide/mixed metal oxides, or integrating different pseudocapacitive/battery-type electrodes [9]. Among the transition metals, Ni and Co are rich in valence electrons. Therefore, such metals considerably impact supercapacitors with their rich electrochemical activity. Moreover, their corresponding MTMS, such as NiCo_2S_4 , exhibit superior faradaic behavior to those of mono-metallic sulfides counterparts, such as NiS and CoS [10–12], and higher electrical conductivity than bimetallic NiCo_2O_4 [13]. In addition, the 2D layered compound of Mo, such as MoS_2 , has both the metallic 1T phase and the semiconducting 2H phase [14,15]. Such 2D material also has a small bandgap of 1.2~1.9 eV that can be used in nanoelectronics [16]. It is important to note that the characteristics of MoS_2 are similar to another carbonaceous 2D material, i.e., graphene. However, MoS_2 has better capacitive characteristics than graphene. It also displays faster intrinsic ionic conductivity than oxides [17,18].

In the present work, NiCo_2S_4 is combined with MoS_2 to develop a hybrid supercapacitor device. Herein, MoS_2 is chosen as one of the components as the bulk MoS_2 is composed of metallic Mo-layers sandwiched between two sulfur layers held together by weak van der Waals interactions. Hence, the electrolyte ions can diffuse quickly and intensely into the material and increase the electrochemical charge storage properties. Interestingly, NiCo_2S_4 only uses the anions of the electrolyte in the charging process, whereas MoS_2 uses the cations of the electrolyte during the discharge process. Later, such charge–discharge characteristics tend to enhance the overall electrochemical properties of the supercapacitors. Benefiting from the MS and MTMS, the electrode exhibited excellent C_{sp} after 45,000 charge/discharge cycles. Moreover, the corresponding hybrid device demonstrated good cycling stability over 15,000 cycles and decent E_D .

2. Experimental Section

Synthesis of NiCo_2S_4 - MoS_2 Composites

The NiCo_2S_4 - MoS_2 composite was synthesized by the one-step solvothermal approach. The precursors, 0.3 g $\text{Ni}(\text{NO}_3)_2$, 0.6 g $\text{Co}(\text{NO}_3)_2$, 2 mL $\text{C}_2\text{H}_8\text{N}_2$ (ethylenediamine), 0.8 g $\text{C}_2\text{H}_5\text{NS}$ (thioacetamide), and different amounts (0.05 and 0.15 g) of Na_2MoO_4 were dissolved and mixed in 30 mL $\text{C}_2\text{H}_6\text{O}_2$ (ethylene glycol) with constant stirring and shifted to a Teflon-lined autoclave. The solution-filled autoclave was heated at 200 °C for 15 h and then cooled down. After the completion of the reaction, the material was filtered, washed, and dried at 60 °C for 12 h. Two composites with dissimilar morphologies called NCMS-L (NiCo_2S_4 / MoS_2 with low Mo content) (sheet-like) and NCMS-H (NiCo_2S_4 / MoS_2 high with Mo content) (rod-like) were produced using low (0.05 g) and high (0.15 g) amounts of Na_2MoO_4 , respectively.

Furthermore, bare NiCo_2S_4 and bare MoS_2 were also synthesized using the above-mentioned procedures in the absence of Mo^{6+} for bare NiCo_2S_4 and Ni^{2+} and Co^{2+} for bare MoS_2 , respectively.

3. Results and Discussion

3.1. Synthesis Mechanism of NiCo_2S_4 / MoS_2 Composite

The current work is focused on developing two different morphologies of the composite of NiCo_2S_4 and MoS_2 . A schematic diagram demonstrates the formation mechanism of these two morphologies (Figure 1). Initially, $\text{Ni}(\text{NO}_3)_2$, $\text{Co}(\text{NO}_3)_2$, and Na_2MoO_4 were dissolved in ethylene glycol to form Ni^{2+} , Co^{2+} , and MoO_4^{2-} ions. It is important to note that the rapid transportation of MoO_4^{2-} was restricted by its high molar mass and the high viscosity of ethylene glycol solvent. Additionally, the formation of stable NiCo_2S_4 took longer time than MoS_2 . Therefore, MoO_4^{2-} was first combined with H_2S to form amorphous MoS_2 . Therefore, no apparent peaks of MoS_2 are observed in the XRD patterns of the composite materials (Figure 2a–c). With the assistance of the $-\text{NH}_2$ group in thioacetamide, Ni^{2+} and Co^{2+} formed stable complexes on the surface of MoS_2 and then reacted with H_2S to produce NiCo_2S_4 [19]. On the other hand, the morphology of composite material changed from sheet-like to rod-like by increasing the concentration

of the precursor $\text{Na}_2\text{MoO}_4 \cdot 2\text{H}_2\text{O}$ from 0.05 g to 0.15 g (Figure 3a–d). Probable reactions during the solvothermal process are shown below:

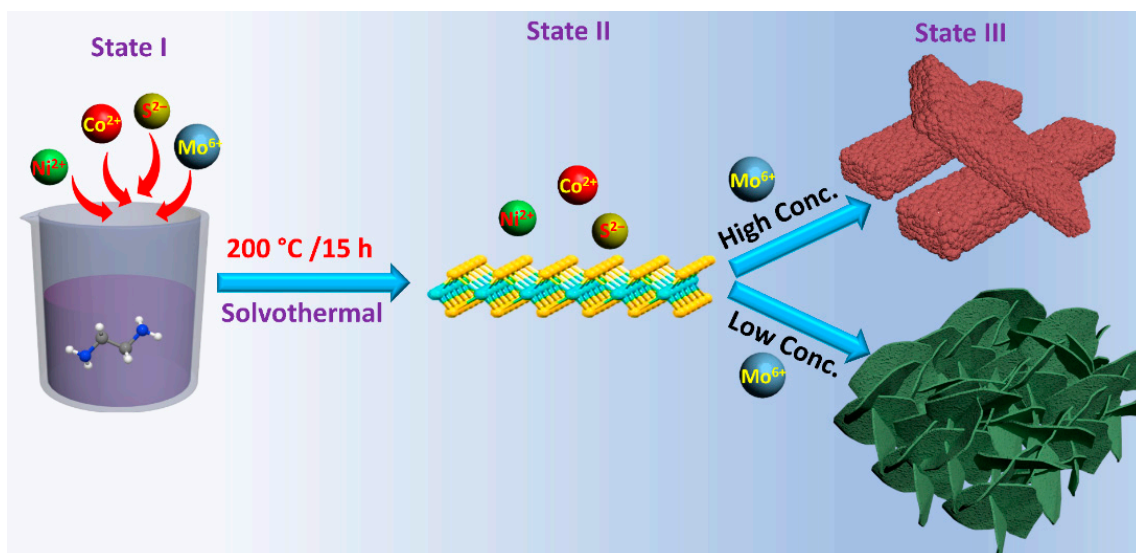
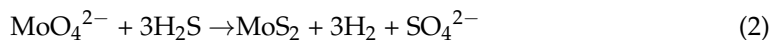


Figure 1. Schematic diagram of the NCMS (State I demonstrates the mixing of all precursors. State II designates the formation of MoS_2 . State III demonstrates the formation of NiCo_2S_4 over MoS_2 with sheet- and rod-like morphologies).

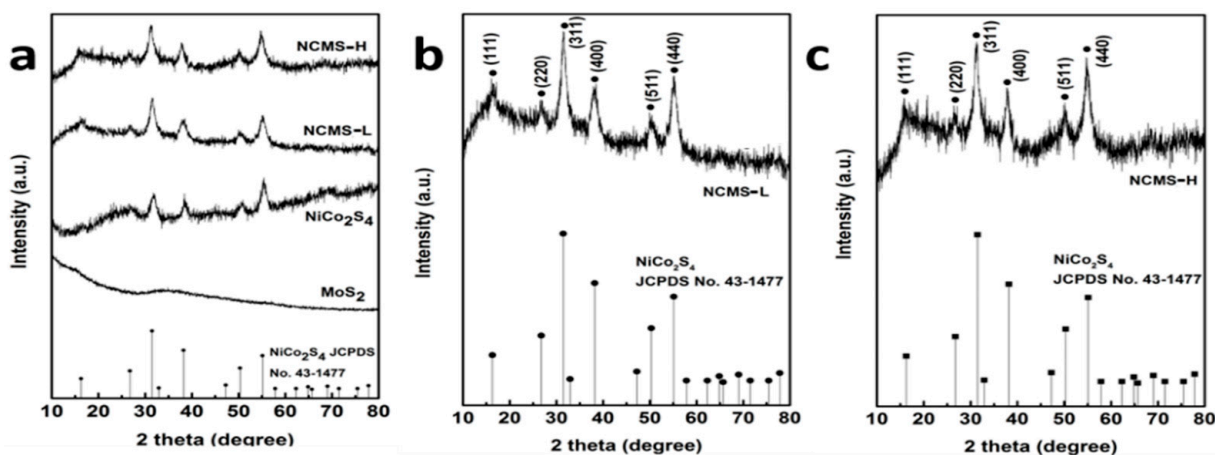


Figure 2. XRD patterns of the composite material NCMS-L, NCMS-H, NiCo_2S_4 , and MoS_2 (a); XRD patterns of NCMS-L (b) and NCMS-H (c).

The change in morphology with altering the concentration of MoO_4^{2-} can be attributed to the change in the direction of diffusion of MoO_4^{2-} during its ion-exchange process with S^{2-} . The inward diffusion of MoO_4^{2-} produced sheet-like morphology, whereas the outward diffusion resulted in the synthesis of a rod-like composite [20].

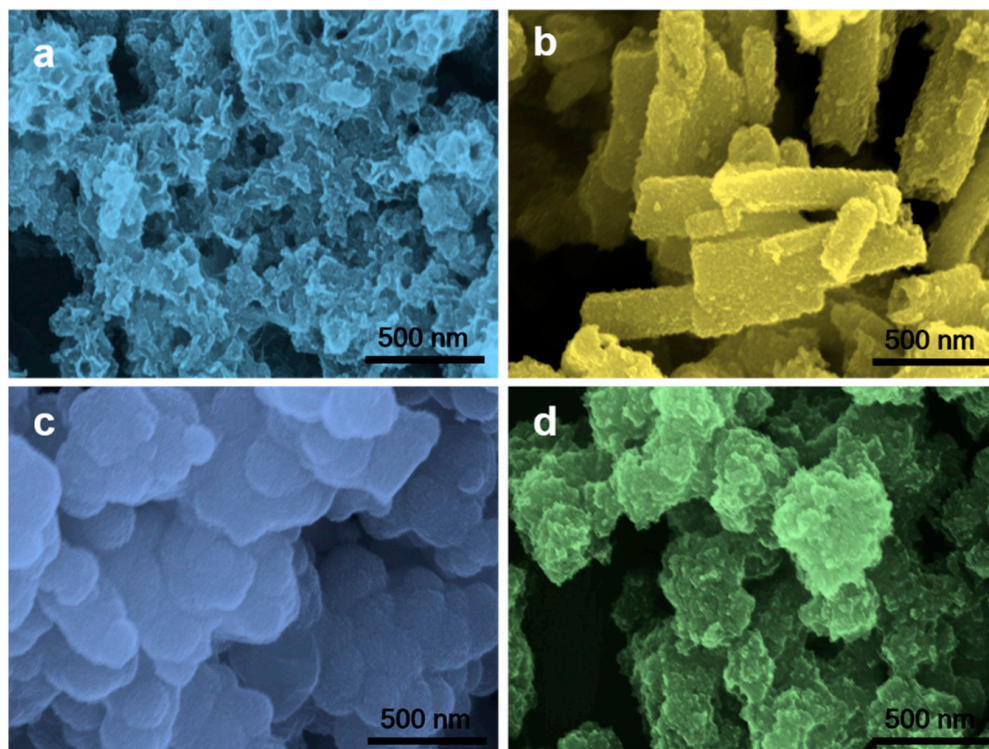


Figure 3. High-magnification SEM images of (a) NCMS-L, (b) NCMS-H, (c) MoS₂, and (d) NiCo₂S₄.

3.2. Characterization and Morphology of NiCo₂S₄/MoS₂ Composite

The crystallinity of composite materials was examined by XRD analysis (Figure 2a–c). The XRD pattern of bare NiCo₂S₄ demonstrates all the characteristic peaks for the NiCo₂S₄ phase (JCPDS card No. 43-1477). On the other hand, for NCMS-L, the XRD peaks are observed at 17.02, 26.82, 31.54, 37.76, 50.23, and 55.12° 2θ, corresponding to the (111), (220), (311), (400), (511), and (440) planes of NiCo₂S₄, respectively (Figure 2b). However, the HRTEM analysis reveals the presence of the (002) plane of MoS₂, according to the JCPDS card No.37-1492 (Figure S1). Moreover, the concentration of precursor Mo⁶⁺ was low compared to Ni²⁺ and Co²⁺, which generates dominant peaks of NiCo₂S₄ to suppress the peaks of MoS₂. The XRD pattern of bare amorphous MoS₂ confirms the amorphous nature (Figure 2a). In addition, the absence of any secondary peak in the XRD pattern of the composites indicates their high purity. A similar XRD pattern has also been observed for NCMS-H (Figure 2c). The morphologies of bare NiCo₂S₄ and MoS₂ and their composites were analyzed by FESEM, as shown in Figure 3a–d. Both bare NiCo₂S₄ and MoS₂ display the presence of aggregated clusters. However, compared with MoS₂, NiCo₂S₄ shows bigger clusters. On the other hand, composite materials NCMS-L and NCMS-H exhibit sheet-like morphology, respectively. From the morphological analysis, it is confirmed that NCMS-L displays higher porosity than NCMS-H. This fact also explains why the capacitance retention of NCMS-L was better than NCMS-H after cycling tests (Figures 7d and S6d) [13,21,22]. Furthermore, TEM analysis was performed to examine the microstructure of the electrode materials. As shown in Figure 4a, NCMS-L displays a porous sheet-like structure. On the contrary, NCMS-H shows a rod-like structure (Figure 4b). Therefore, it is essential to note that the SEM images support the TEM analysis result. On the other hand, Figure 4c,d shows the structure of MoS₂ and NiCo₂S₄, respectively. However, the NiCo₂S₄ particles are found to be larger and denser than MoS₂. Owing to the small-sized particles and amorphous structure of MoS₂, the electrolyte can pass easily inside the composite material and enhance the redox reaction to deliver high C_{sp}.

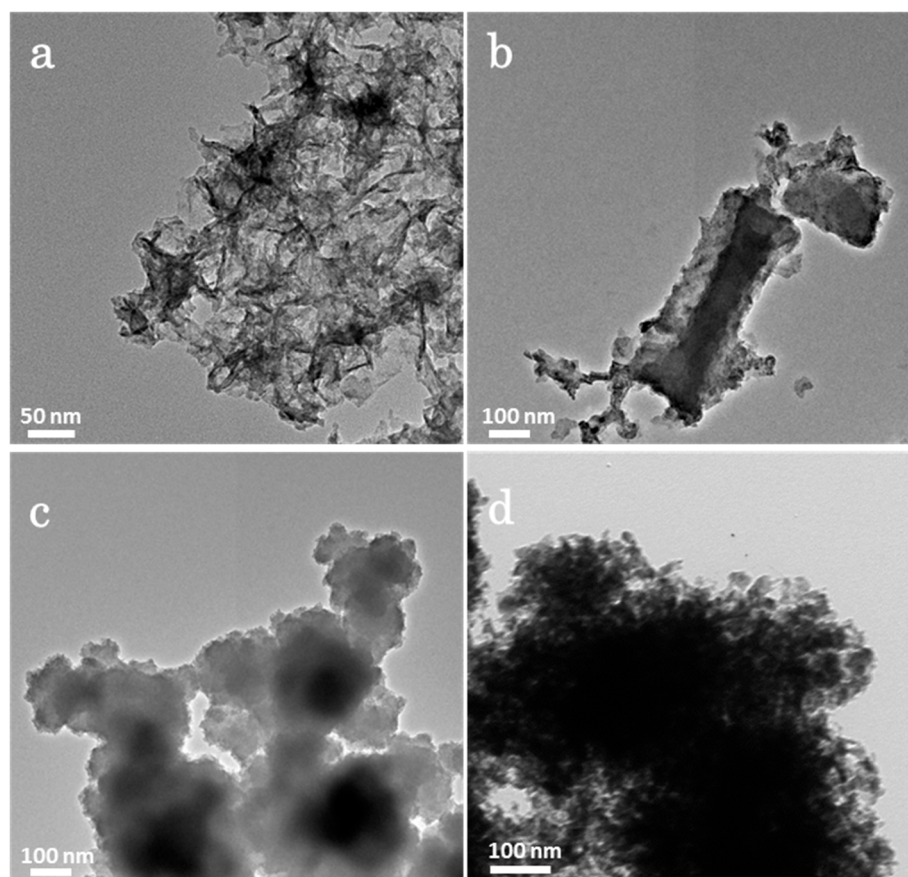


Figure 4. TEM images of (a) NCMS-L, (b) NCMS-H, (c) MoS₂, and (d) NiCo₂S₄.

The elemental composition and chemical state in NCMS-L were evaluated by XPS, as presented in Figure 5a–e. The survey spectrum confirms the presence of metal components and the other corresponding elements, such as O and S (Figure 5a). The deconvoluted Ni 2p core-level spectrum shows four peaks. Herein, two spin-orbit doublets correspond to Ni²⁺ and Ni³⁺ [23]. Furthermore, two shake-up satellites (identified as “Sat.”) have also been observed (Figure 5b). On the other hand, two spin-orbit doublets in Co 2p spectrum can be designated as Co²⁺ and Co³⁺ [24]. Moreover, one shake-up satellite has also been observed (Figure 5c). The S 2p spectrum is deconvoluted into two significant peaks and a shake-up satellite peak with binding energies of 162.8 and 161.6 eV, corresponding to S 2p_{1/2} and S 2p_{3/2}, respectively, as shown in Figure 5e [25].

The Mo 3d XP spectrum in Figure 5d shows two strong peaks at 228.8 and 232.4 eV, which can be assigned to the Mo 3d_{5/2} and Mo 3d_{3/2} doublet, respectively. The peak at 226.2 eV is assigned to S 2s [20]. Furthermore, to determine the presence of Mo in the composite material, EDX elemental mapping was performed for NCMS-L through HR-TEM analysis (Figures 6 and S2). As expected, the concentration of Mo is lower than the other elements, Ni, Co, and S. However, all elements are distributed uniformly. From EDX analysis, it can be concluded that MoS₂ can cooperate and enhance the electrochemical properties of NiCo₂S₄ to obtain promising electrochemical performance.

3.3. Electrochemical Properties of NiCo₂S₄/MoS₂ Nanocomposite

The CV (cyclic voltammetry), GCD (galvanostatic charge/discharge), and EIS (electrochemical Impedance Spectroscopy) tests were performed to explore the electrochemical properties of NCMS-L, NCMS-H, bare MoS₂, and bare NiCo₂S₄ electrodes in a 3 M KOH electrolyte. Figure 7a represents the CV curves of NCMS-L within the potential limit of 0 to 0.6 V at various scan rates of 5–100 mV s^{−1}. The CV curves reveal faradaic behavior,

in which a pair of prominent redox peaks are observed. Similarly, NiCo₂S₄ and MoS₂ electrodes also have a pair of redox peaks at different scan rates (Figures S4 and S5). The corresponding redox reactions can be expressed as follows [14,15,21,26–30]:

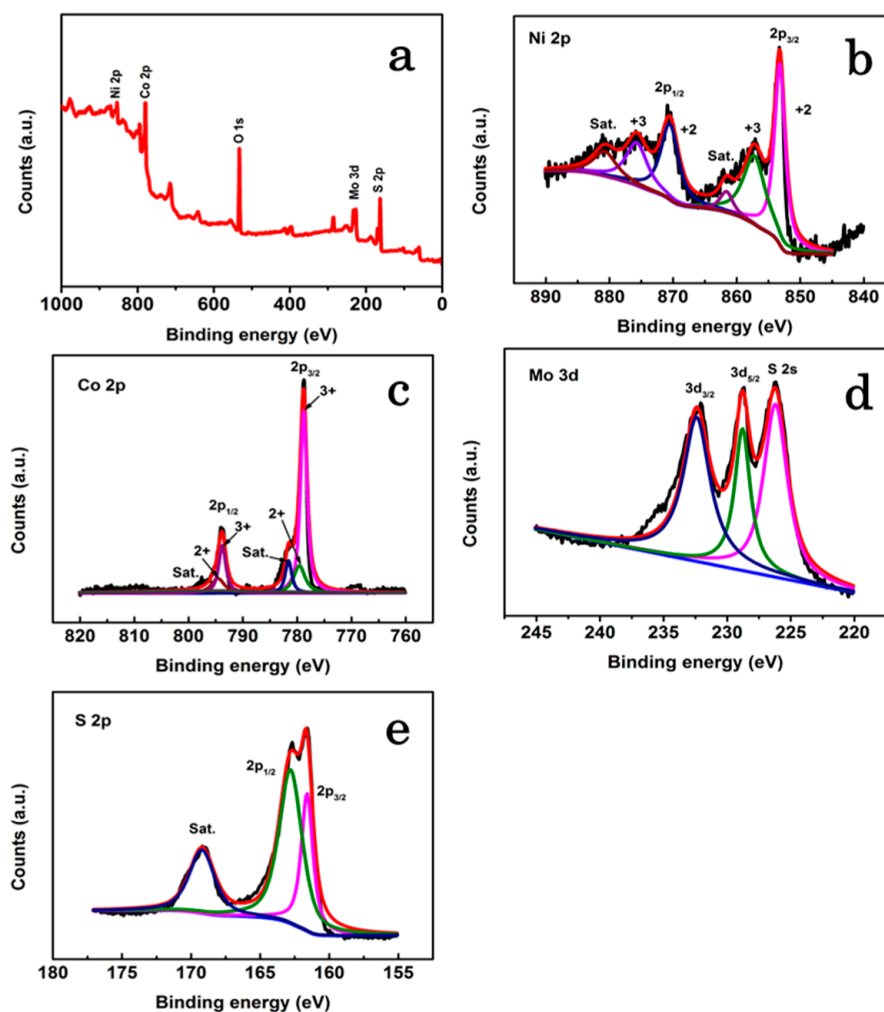


Figure 5. XPS analysis of NCMS-L: (a) Survey XPS pattern, high-resolution XPS spectra of (b) Ni 2p, (c) Co 2p, (d) Mo 3d, and (e) S 2p.

The GCD test of NCMS-L, bare NiCo₂S₄, and bare MoS₂ are performed at the constant currents of 1, 3, 5, 8, and 10 mA (or corresponding current densities of 0.8, 2.3, 3.8, 6.2, and 7.7 A g⁻¹). Based on the GCD and CV curves, the C_{sp} of the electrodes was calculated using the following equations:

$$C_s = \frac{It}{m\Delta V} \quad (9)$$

$$C_s = \frac{\int i(V)dV}{2vm\Delta V} \quad (10)$$

where I is the response constant current (A); t is the discharge time (s); ΔV is the potential window of the CV or GCD curves (V); m is the mass of active material (g); i and V are current and potential in the CV curve (A and V), respectively, and ν is the scan rate ($V s^{-1}$) [31].

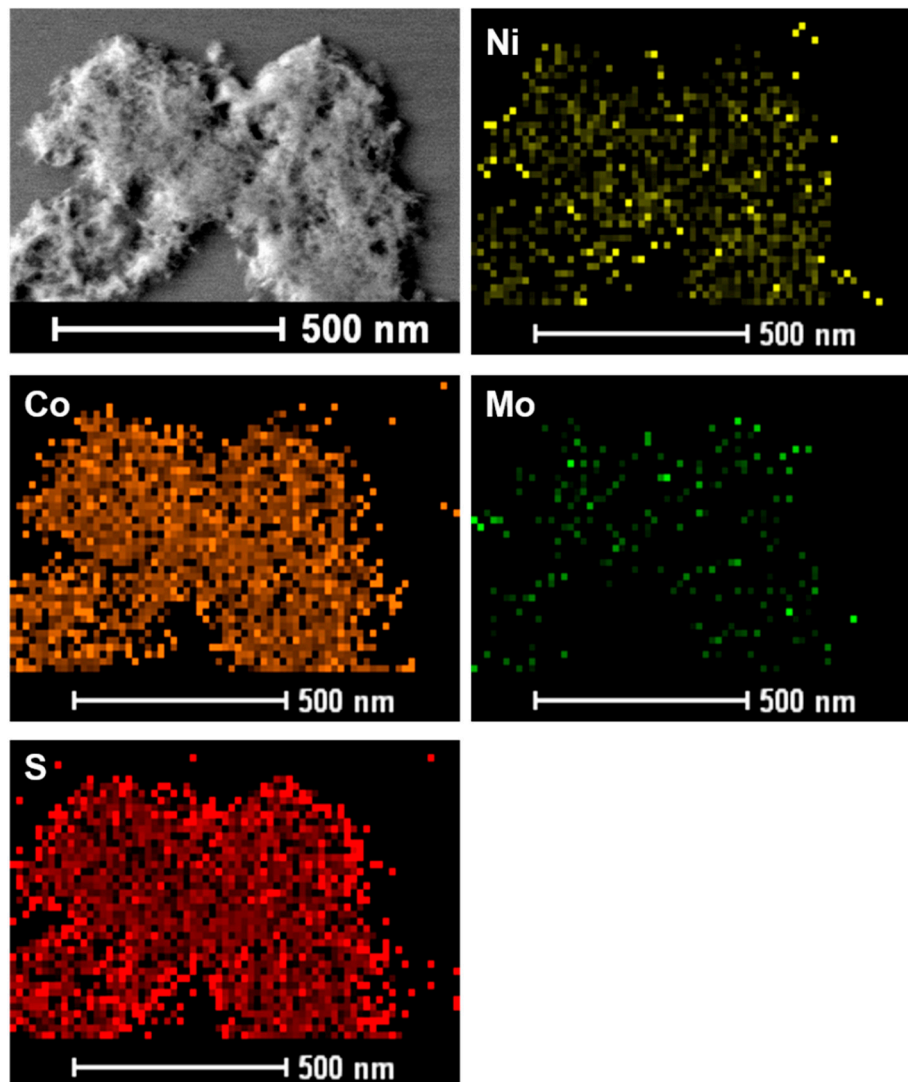


Figure 6. EDX element mapping images of NCMS-L indicating the elemental distribution of Ni, Co, Mo, and S.

The C_{sp} of NCMS-L was calculated to 1390, 1000, 864, 756, and 698 $F g^{-1}$ at the currents of 1, 3, 5, 8, and 10 mA (corresponding current densities of 0.8, 2.3, 3.8, 6.2, and 7.7 $A g^{-1}$), respectively (Figure 7b). It is important to note that the GCD profiles indicate significant deviation from the ideal rectangular shapes, indicating the Faradaic characteristics. The cycling stability of the electrode was assessed by continuing the CV test for 45,000 cycles at the scan rate of 100 $mV s^{-1}$, as presented in Figure 7c,d. The electrode exhibited superior capacitance retention of 135% over the first 8000 cycles. However, after these initial cycles, the capacitance retention gradually increased to 149% for up to 35,000 cycles, which is associated with the activation of the electrode material. For further activation of the electrode and to check the electrode's feasibility for long-term stability, the cycling process was stopped for one week with the electrode soaked in the electrolyte solution. The cycling test continued up to the 45,000th cycle. We found that soaking the electrodes in the electrolyte for a long time (after activation) was quite favorable for enhanced cycling stability. Such drastic enhancement in electrochemical performance is associated with the

electrochemical reconstruction of the electrode materials during cycling and soaking the electrode in electrolyte solution for a long time [32]. It is important to note that, after the soaking process, the capacitance retention increased to 207% at the 38,000th cycle, which can be associated with the re-activation of the electrode. However, the capacitance then gradually decreased and reached 192% of its initial capacitance at the 45,000th cycle due to the structural breakdown, as depicted in Figure S3.

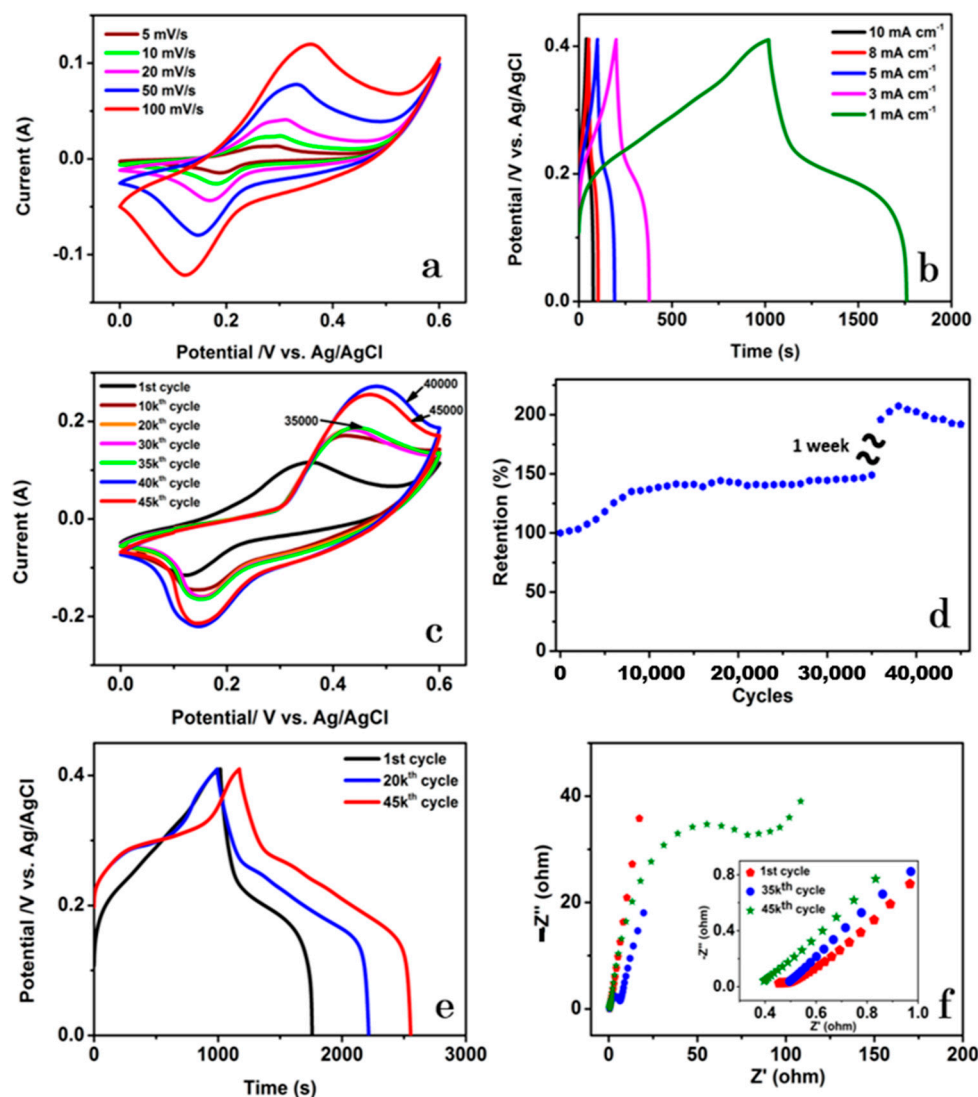


Figure 7. Electrochemical properties of NCMS-L: (a) CV curves at different scan rates, (b) GCD profiles at currents ranging from 1 mA to 10 mA with a current density (CD) of 0.8, 2.3, 3.8, 6.2, and 7.7 A g^{-1} , respectively, (c) CV curves at various cycles with a scan rate of 100 mV s^{-1} , (d) Retention during 45,000 cycles by CV at the scan rate of 100 mV s^{-1} , (e) GCD profiles at various cycles, and (f) Nyquist plots at 1st, 35,000th, and 45,000th cycle.

The cycling stability increased to 207% at the 38,000th cycle; after that, it decreased slightly to 192% at the 45,000th cycle. The GCD test examined the retention of the specific capacitance of NCMS-L at 1 mA (Figure 7e). The C_{sp} was enhanced from 1390 to 2293 F g^{-1} at the 20,000th cycle and 2594 F g^{-1} at the 45,000th cycle. Moreover, the coulombic efficiency increased from 73% to 123% at the 20,000th cycle and then slightly decreased to 118% at the 45,000th cycle. Figure 4f shows the corresponding Nyquist plots at the 1st, 35,000th, and 45,000th cycles. The intercept at the y -axis in the high-frequency region that signifies the equivalent series resistance (ESR) was 0.45Ω (1st cycle), 0.49Ω (35,000th cycle), and 0.39Ω (45,000th cycle), respectively. The increase and decrease in ESR over the cycles are

agreed well with the change in capacitance over the long-term cycling stability. Similar trends have also been found for NiCo_2S_4 and MoS_2 , as shown in Figures S4c and S5c.

Comparing CV curves of MoS_2 , NiCo_2S_4 , and NCMS-L at a scan rate of 100 mV s^{-1} displays the highest current response for the composite (Figure 8a). The comparative GCD plots at the current of 1 mA also designate a higher discharge time of NCMS-L than its monometallic and bimetallic counterparts (Figure 8b). Figure 8c represents the CV curves of NiCo_2S_4 at different cycles at the constant scan rate of 100 mV s^{-1} . Compared to the 1st cycle, a significant change in CV pattern is observed at the 5000th cycle. This fact indicates the gradual activation of the electrode material. However, the CV curves' redox characteristics do not alter after 1000 cycles, indicating good electrochemical stability. Most importantly, the electrode displayed a good cycling stability of 147% after 5000 cycles (Figure 8d). A similar pattern has also been observed for the MoS_2 electrode (Figure 8e). Nevertheless, the MoS_2 displayed better cycling stability (248%) than NiCo_2S_4 over 5000 cycles (Figure 8f). Similar to other supercapacitor electrodes, the area under the CV profiles increases with increasing the scan rate for NiCo_2S_4 (Figure S4a). The faradaic charge storage characteristics are visible from the GCD profiles at different current densities (Figure S4b). It is important to note that the discharge time was increased after 5000 cycles (Figure S4d).

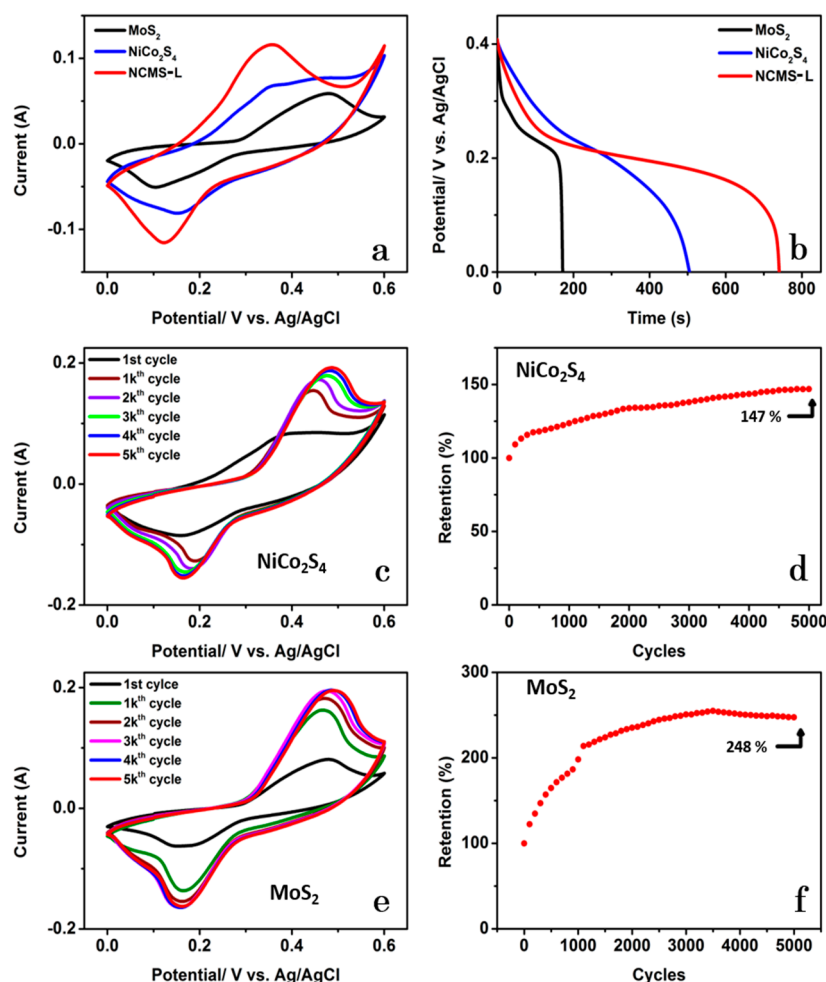


Figure 8. (a) Comparative CV curves of MoS_2 , NiCo_2S_4 , and NCMS-L at a scan rate of 100 mV s^{-1} , (b) GCD curves of MoS_2 , NiCo_2S_4 , and NCMS-L at 1 mA (CD of 0.8 A g^{-1}); CV curves of (c) NiCo_2S_4 and (e) MoS_2 at various cycles at a scan rate of 100 mV s^{-1} ; (d,f) Retention of NiCo_2S_4 and MoS_2 after 5000 cycles by CV with a scan rate of 100 mV s^{-1} .

Likewise, the capacitance of NiCo_2S_4 was increased from 947 to 1121 F g^{-1} after 5000 cycles. Figure S5a–d represents the electrochemical data for MoS_2 . Similar to NiCo_2S_4 ,

the faradaic charge storage ability of MoS₂ is visible from their CV curves and GCD profiles (Figure S5a,b). However, the cycling stability of MoS₂ drastically increased from 323 to 1100 F g⁻¹ after 5000 cycles. Overall, MoS₂, NiCo₂S₄, and NCMS-L showed the C_{sp} of 323, 947, and 1390 F g⁻¹, respectively. The better capacitive performance of NCMS-L can be ascribed to the strong synergistic contribution of its components, i.e., MoS₂ and NiCo₂S₄. For NCMS-L, Ni²⁺ and Co³⁺ are combined with OH⁻ to produce Ni³⁺ and Co⁴⁺ during charging. However, K⁺ is inserted into the active material and has a redox reaction on the surface of MoS₂ during discharging [15]. These results explain the increase in C_{sp} of NCMS-L and a considerable increase in the coulombic efficiency from 73% to 123% over 20,000 cycles. On the other hand, it takes a long time for K⁺ ions to penetrate the structure of NCMS-L and have a redox reaction with MoS₂. After 35,000 cycles, the cycling process was suspended for one week to ensure the complete diffusion of the electrolyte ions into the active material, obtaining enhanced capacitance retention of 192%.

To understand the individual contributions of NiCo₂S₄ and MoS₂ on the cycling stability of NCMS-L, an EIS analysis was performed. After 5000 cycles, the ESR of bare NiCo₂S₄ increased from 0.53 to 0.6 Ω (Figure S4c), whereas it decreased from 1.86 to 0.58 Ω for bare MoS₂ (Figure S5c). The significant decrease in ESR for MoS₂ is well supported by the substantial enhancement of discharge time, as shown in Figure S5d. The morphological analysis of these electrodes after the cycle test reveals a significant change in the structure of MoS₂ from clusters to coral (Figure S3b). However, no significant change in morphology has been observed for NiCo₂S₄ (Figure S3c).

Interestingly, during the pause of the cycling test for two weeks, the morphology of MoS₂ was further changed from coral to chunks (Figure S7a). However, no significant change in the morphology of NiCo₂S₄ has been observed after the pause of the cycle test (Figure S7b). This phenomenon indicates that MoS₂ undergoes drastic structural reformation during the cycling test as well as during the pause of the cycle test. This fact also supports the electrochemical reconstruction of NCMS-L during the cycle test. Therefore, it can be concluded that MoS₂ has majorly contributed to the enhanced electrochemical performance of NCMS-L over long-term cycle life. The enhanced cycling stability of MoS₂ is the driving force of such boosted cycling stability of the composite.

To further estimate the prospective of the NCMS-L electrode for practical applications, an asymmetric supercapacitor device was designed with activated carbon (AC) as the negative electrode, NCMS-L as the positive electrode, and a 3 M KOH aqueous solution as the electrolyte.

The mass of the negative and positive electrodes was adjusted based on the charge balance theory ($q^+ = q^-$), as shown in the following equation:

$$q = I\Delta t = C_s m \Delta V \quad (11)$$

Therefore, the mass ratio of the electrode materials was calculated using Equation (12).

$$\frac{m^+}{m^-} = \frac{C_s^- \Delta V^-}{C_s^+ \Delta V^+} \quad (12)$$

where C_s , ΔV , and m are the C_{sp}, potential window, and mass of active materials, respectively. The mass ratio of NCMS-L and AC was 0.26, and the total mass of the two electrodes was 6.3 mg.

Figure 9a represents the CV curves of the NCMS-L//AC hybrid supercapacitor device within potential limit of 0 to 1.6 V at different scan rates from 5 to 100 mV s⁻¹. The CV curves indicate the presence of redox peaks, indicating the Faradaic charge storage mechanism. Figure 9b presents the GCD profiles at various current densities of 0.16, 0.32, 0.47, 0.79, 1.27, and 1.59 A g⁻¹, respectively. The maximum C_{sp} of the device was calculated to be 90 F g⁻¹ at a CD of 0.16 A g⁻¹. The device also delivered a high-rate capability of 64% after a 10-fold increase in the CD (Figure 9c). As shown in Figure 9d, the device exhibited a long cycle life over 15,000 cycles, which is better than some of the reported devices

(Table S1). The device retained 111% of its initial capacitance during the first 1500 cycles. The initial increase in capacitance can be attributed to the steady activation of electrode material. The device exhibited a capacitance retention of 102% after 15,000 cycles. Moreover, it also displayed 98% retention of its initial coulombic efficiency after 15,000 cycles. The enhanced cycling stability of the device can be ascribed to the porous nature of the positive electrode, the synergistic contribution of the individual components of the composite, and the better chemical stability of the carbon black (negative electrode). The device also displayed higher E_D than the other related devices, as shown in the Ragone plot (Figure 9e) [13,33–35]. Based on the equations, $E_D = 0.5 CV^2$ and $P_D = E_D/t$, the maximum E_D was calculated to be 31.9 Wh kg^{-1} at a P_D of 0.13 kW kg^{-1} , and the highest P_D was 1.26 kW kg^{-1} at the corresponding E_D of 20.7 Wh kg^{-1} . The ESR of the device in the first cycle was approximately reduced to half that of the three-electrode system with a value of 0.22Ω . However, it was further increased to 0.32Ω after 15,000 cycles (Figure 9f).

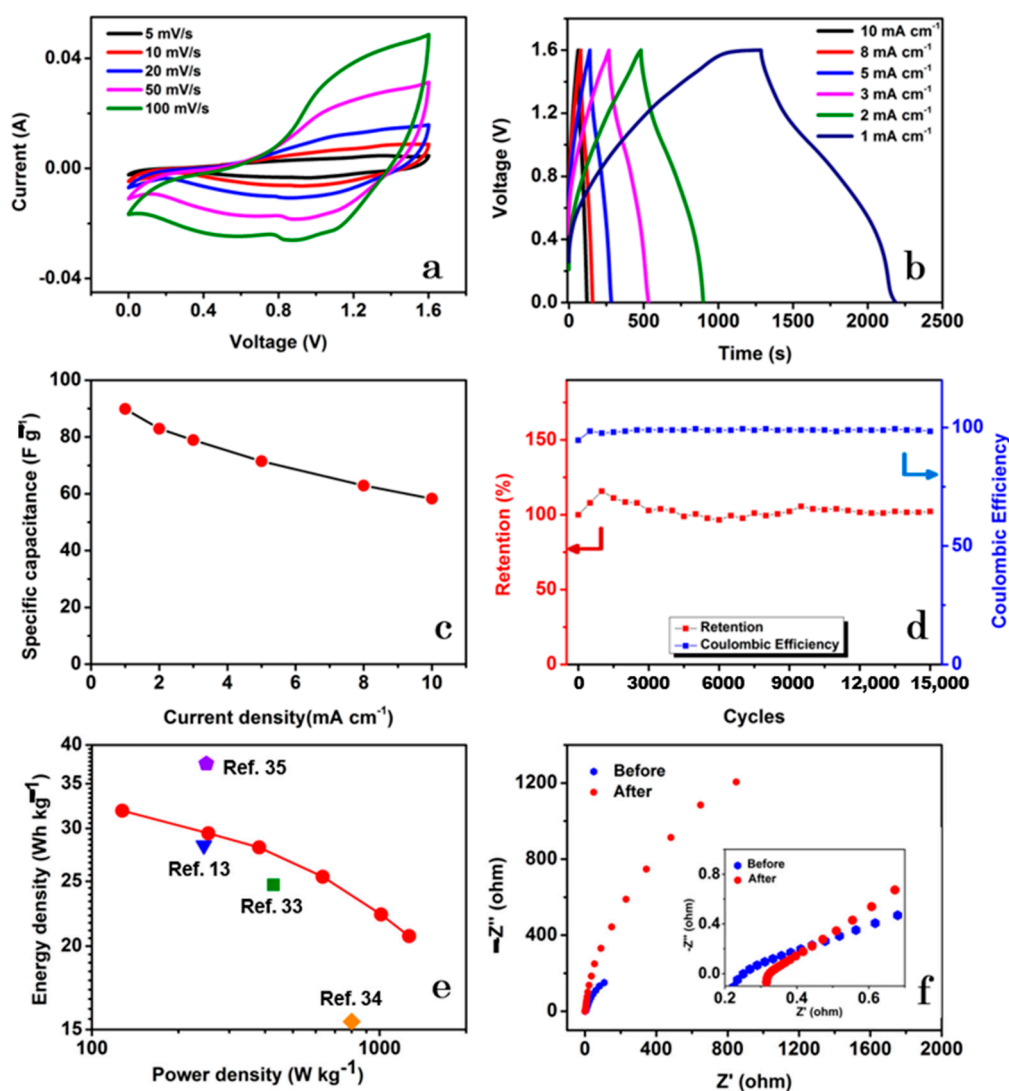


Figure 9. Electrochemical performance of the hybrid supercapacitor device of NCMS-L and activated carbon: (a) CV profiles at various scan rates, (b) GCD curves at different currents from 1 mA to 10 mA with a CD of 0.16, 0.32, 0.47, 0.79, 1.27, and 1.59 A g⁻¹, respectively, (c) variation of C_{sp} with the change in current densities, (d) capacitance retention during 15,000 cycles at the CD of 6.35 A g⁻¹, (e) the Ragone plot, and (f) Nyquist plots at the frequency range of 0.01 Hz to 100 kHz before and after 15,000 cycles.

The electrode displayed decent capacitance, low ESR, and enhanced cycling stability. Such enhanced electrochemical performance of NCMS-L can be attributed to the following factors:

1. The synergistic contribution of each composite component is highly responsible for such enhanced electrochemical performance. The combination of highly capacitive NiCo_2S_4 and highly conductive MoS_2 is feasible for fabricating high-performance supercapacitor electrodes.
2. The enhanced cycling stability of the composite can be attributed to its electrochemical reconstruction during the cycling test.
3. The porous morphology of the composite (NCMS-L) is favorable for the easy transport of electrolyte ions during the electrochemical test.
4. The enhanced mechanical strength of MoS_2 restricted the structural deformation of the electrode during the long-term cycling test.

4. Conclusions

Advanced composite electrodes based on NiCo_2S_4 and MoS_2 with different morphologies have been synthesized through facile solvothermal processes. Benefiting from a rich faradaic charge storage mechanism, the electrodes displayed a promising electrochemical performance in high capacitance and low ESR. Nevertheless, the composite electrode also exhibited long-term cycle life with negligible capacitance fading. Overall, this composite material can be designated one of the striking candidates for future energy storage devices.

Supplementary Materials: The following are available online at <https://www.mdpi.com/article/10.3390/nano13040689/s1>, Experimental section, Figure S1: HRTEM image of NCMS-L sample, Figure S2: EDX of NCMS-L sample; Figure S3: SEM images of NCMS-L after 45,000 cycles and of MoS_2 and NiCo_2S_4 after 5000 cycles; Figures S4–S6: electrochemical properties of NiCo_2S_4 , MoS_2 , NCMS-H, Figure S7: SEM images of MoS_2 and NiCo_2S_4 after 5000 cycles and two weeks' pause; Table S1: comparison of the C_{sp} , E_D , P_D , and stability of the $\text{NiCo}_2\text{S}_4/\text{MoS}_2//\text{AC}$ devices with other related devices; References [13,33–35] are cited in the Supplementary Materials.

Author Contributions: Conceptualization, formal analysis, investigation, data curation, writing—original draft, L.N.M.T.; formal analysis, data curation, writing—review and editing, S.S.; visualization, software, G.D.; writing—review and editing, V.H.N.; validation, J.L.; validation, Y.R.L.; resources, supervision, project administration, funding acquisition, writing—review and editing, J.-J.S. All authors have read and agreed to the published version of the manuscript.

Funding: This study was supported by the National Research Foundation (NRF) of the Republic of Korea under the frameworks of the Priority Research Centers Program (NRF-2014R1A6A1031189) and the Regional University Superior Scientist Research Program (NRF-2020R1I1A3073981) funded by the Ministry of Education, the Republic of Korea.

Data Availability Statement: The data presented in this study are available in the lab research notebook at Yeungnam University.

Conflicts of Interest: The authors declare no conflict of interest.

References

1. Simon, P.; Gogotsi, Y. Materials for electrochemical capacitors. *Nat. Mater.* **2008**, *7*, 845–854. [[CrossRef](#)]
2. Sahoo, S.; Dhakal, G.; Kim, W.K.; Shim, J.J. Ternary Nanohybrid of $\text{Ni}_3\text{S}_2/\text{CoMoS}_4/\text{MnO}_2$ on Nickel Foam for Aqueous and Solid-State High-Performance Supercapacitors. *Nanomaterials* **2022**, *12*, 1945. [[CrossRef](#)] [[PubMed](#)]
3. Dhakal, G.; Mohapatra, D.; Kim, Y.I.; Lee, J.; Kim, W.K.; Shim, J.J. High-performance supercapacitors fabricated with activated carbon derived from lotus calyx biowaste. *Renew. Energy* **2022**, *189*, 587–600. [[CrossRef](#)]
4. Sahoo, S.; Kumar, R.; Joanni, E.; Singh, R.K.; Shim, J.J. Advances in pseudocapacitive and battery-like electrode materials for high performance supercapacitors. *J. Mater. Chem. A* **2022**, *10*, 13190–13240. [[CrossRef](#)]
5. Sahoo, S.; Shim, J.J. Facile synthesis of three-dimensional ternary $\text{ZnCo}_2\text{O}_4/\text{reduced graphene oxide}/\text{NiO}$ composite film on nickel foam for next generation supercapacitor electrodes. *ACS Sustain. Chem. Eng.* **2017**, *5*, 241–251. [[CrossRef](#)]
6. Halper, M.S.; Ellenbogen, J.C. *Supercapacitors: A Brief Overview*; MITRE Nanosystems Group: McLean, VA, USA, 2006.

7. Conway, B.E. *Electrochemical Supercapacitors: Scientific Fundamentals and Technological Applications*; Springer Science & Business Media: Berlin/Heidelberg, Germany, 2013.
8. Yan, J.; Wang, Q.; Wei, T.; Fan, Z. Supercapacitors: Recent Advances in Design and Fabrication of Electrochemical Supercapacitors with High Energy Densities. *Adv. Energy Mater.* **2014**, *4*, 1300816. [[CrossRef](#)]
9. Brousse, T.; Bélanger, D.; Long, J.W. To be or not to be pseudocapacitive? *J. Electrochem. Soc.* **2015**, *162*, A5185–A5189. [[CrossRef](#)]
10. Bulakhe, R.N.; Sahoo, S.; Nguyen, T.T.; Lokhande, C.D.; Roh, C.; Lee, Y.R.; Shim, J.-J. Chemical synthesis of 3D copper sulfide with different morphologies for high performance supercapacitors application. *RSC Adv.* **2016**, *6*, 14844–14851. [[CrossRef](#)]
11. Nguyen, V.H.; Shim, J.-J. In situ growth of hierarchical mesoporous NiCo₂S₄@MnO₂ arrays on nickel foam for high-performance supercapacitors. *Electrochim. Acta* **2015**, *166*, 302–309. [[CrossRef](#)]
12. Dai, Z.; Zang, X.; Yang, J.; Sun, C.; Si, W.; Huang, W.; Dong, X. Template Synthesis of Shape-Tailorable NiS₂ Hollow Prisms as High-Performance Supercapacitor Materials. *ACS Appl. Mater. Interfaces* **2015**, *7*, 25396–25401. [[CrossRef](#)]
13. Zhu, Y.; Wu, Z.; Jing, M.; Yang, X.; Song, W.; Ji, X. Mesoporous NiCo₂S₄ nanoparticles as high-performance electrode materials for supercapacitors. *J. Power Sources* **2015**, *273*, 584–590. [[CrossRef](#)]
14. Acerce, M.; Voiry, D.; Chhowalla, M. Metallic 1T phase MoS₂ nanosheets as supercapacitor electrode materials. *Nat. Nanotechnol.* **2015**, *10*, 313–318. [[CrossRef](#)] [[PubMed](#)]
15. Mahmood, Q.; Park, S.K.; Kwon, K.D.; Chang, S.-J.; Hong, J.-Y.; Shen, G.; Jung, Y.M.; Park, T.J.; Khang, S.W.; Kim, W.S.; et al. Transition from Diffusion-Controlled Intercalation into Extrinsic Pseudocapacitive Charge Storage of MoS₂ by Nanoscale Heterostructuring. *Adv. Energy Mater.* **2016**, *6*, 1501115. [[CrossRef](#)]
16. Eda, G.; Yamaguchi, H.; Voiry, D.; Fujita, T.; Chen, M.; Chhowalla, M. Photoluminescence from Chemically Exfoliated MoS₂. *Nano Lett.* **2011**, *11*, 5111–5116. [[CrossRef](#)] [[PubMed](#)]
17. da Silveira Firmiano, E.G.; Rabelo, A.C.; Dalmascio, C.J.; Pinheiro, A.N.; Pereira, E.C.; Schreiner, W.H.; Leite, E.R. Supercapacitor Electrodes Obtained by Directly Bonding 2D MoS₂ on Reduced Graphene Oxide. *Adv. Energy Mater.* **2014**, *4*, 1301380. [[CrossRef](#)]
18. Fan, L.-Q.; Liu, G.-J.; Zhang, C.-Y.; Wu, J.-H.; Wei, Y.-L. Facile one-step hydrothermal preparation of molybdenum disulfide/carbon composite for use in supercapacitor. *Int. J. Hydrogen Energy* **2015**, *40*, 10150–10157. [[CrossRef](#)]
19. Peng, S.; Li, L.; Li, C.; Tan, H.; Cai, R.; Yu, H.; Mhaisalkar, S.; Srinivasan, M.; Ramakrishna, S.; Yan, Q. In situ growth of NiCo₂S₄ nanosheets on graphene for high-performance supercapacitors. *Chem. Commun.* **2013**, *49*, 10178–10180. [[CrossRef](#)]
20. Jia, Y.; Ma, Y.; Lin, Y.; Tang, J.; Shi, W.; He, W. In-situ growth of hierarchical NiCo₂S₄/MoS₂ nanotube arrays with excellent electrochemical performance. *Electrochim. Acta* **2018**, *289*, 39–46. [[CrossRef](#)]
21. Zhang, Y.; Ma, M.; Yang, J.; Sun, C.; Su, H.; Huang, W.; Dong, X. Shape-controlled synthesis of NiCo₂S₄ and their charge storage characteristics in supercapacitors. *Nanoscale* **2014**, *6*, 9824–9830. [[CrossRef](#)]
22. Lin, L.; Liu, J.; Liu, T.; Hao, J.; Ji, K.; Sun, R.; Zeng, W.; Wang, Z. Growth-controlled NiCo₂S₄ nanosheet arrays with self-decorated nanoneedles for high-performance pseudocapacitors. *J. Mater. Chem. A* **2015**, *3*, 17652–17658. [[CrossRef](#)]
23. Hou, L.; Shi, Y.; Zhu, S.; Rehan, M.; Pang, G.; Zhang, X.; Yuan, C. Hollow mesoporous hetero-NiCo₂S₄/Co₉S₈ submicro-spindles: Unusual formation and excellent pseudocapacitance towards hybrid supercapacitors. *J. Mater. Chem. A* **2015**, *5*, 133–144. [[CrossRef](#)]
24. Wang, T.; Guo, Y.; Zhao, B.; Yu, S.; Yang, H.P.; Lu, D.; Fu, X.Z.; Sun, R.; Wong, C.P. NiCo₂O₄ nanosheets in-situ grown on three dimensional porous Ni film current collectors as integrated electrodes for high-performance supercapacitors. *J. Power Sources* **2015**, *286*, 371–379. [[CrossRef](#)]
25. Chen, B.; Liu, E.; He, F.; Shi, C.; He, C.; Li, J.; Zhao, N. 2D sandwich-like carbon-coated ultrathin TiO₂@defect-rich MoS₂ hybrid nanosheets: Synergistic-effect-promoted electrochemical performance for lithium ion batteries. *Nano Energy* **2016**, *26*, 541–549. [[CrossRef](#)]
26. Bissett, M.A.; Kinloch, I.A.; Dryfe, R.A.W. Characterization of MoS₂–Graphene Composites for High-Performance Coin Cell Supercapacitors. *ACS Appl. Mater. Interfaces* **2015**, *7*, 17388–17398. [[CrossRef](#)] [[PubMed](#)]
27. Xiao, J.; Wan, L.; Yang, S.; Xiao, F.; Wang, S. Design Hierarchical Electrodes with Highly Conductive NiCo₂S₄ Nanotube Arrays Grown on Carbon Fiber Paper for High-Performance Pseudocapacitors. *Nano Lett.* **2014**, *14*, 831–838. [[CrossRef](#)]
28. Dong, W.; Wang, X.; Li, B.; Wang, L.; Chen, B.; Li, C.; Li, X.; Zhang, T.; Shi, Z. Hydrothermal synthesis and structure evolution of hierarchical cobalt sulfide nanostructures. *Dalton Trans.* **2011**, *40*, 243–248. [[CrossRef](#)]
29. Li, D.; Gong, Y.; Pan, C. Facile synthesis of hybrid CNTs/NiCo₂S₄ composite for high performance supercapacitors. *Sci. Rep.* **2016**, *6*, 29788. [[CrossRef](#)]
30. Wan, H.; Jiang, J.; Yu, J.; Xu, K.; Miao, L.; Zhang, L.; Chen, H.; Ruan, Y. NiCo₂S₄ porous nanotubes synthesis via sacrificial templates: High-performance electrode materials of supercapacitors. *CrystEngComm* **2013**, *15*, 7649–7651. [[CrossRef](#)]
31. Chen, W.; Fan, Z.; Gu, L.; Bao, X.; Wang, C. Enhanced capacitance of manganese oxide via confinement inside carbon nanotubes. *Chem. Commun.* **2010**, *46*, 3905–3907. [[CrossRef](#)]
32. Wang, H.; Zhang, H.; Zhang, D.; Chen, J.; Zhang, S.; Zhang, S.; Yu, J.; Wu, Q.; Li, Q. Toward Enhanced Electrochemical Performance by Investigation of the Electrochemical Reconstruction Mechanism in Co₂V₂O₇ Hexagonal Nanosheets for Hybrid Supercapacitors. *ACS Appl. Mater. Interfaces* **2022**, *14*, 8106–8114. [[CrossRef](#)]
33. Zhu, Y.; Ji, X.; Wu, Z.; Liu, Y. NiCo₂S₄ hollow microsphere decorated by acetylene black for high-performance asymmetric supercapacitor. *Electrochim. Acta* **2015**, *186*, 562–571. [[CrossRef](#)]

34. Lu, X.-F.; Wu, D.-J.; Li, R.-Z.; Li, Q.; Ye, S.-H.; Tong, Y.-X.; Li, G.-R. Hierarchical NiCo₂O₄ nanosheets@hollow microrod arrays for high-performance asymmetric supercapacitors. *J. Mater. Chem. A* **2014**, *2*, 4706–4713. [[CrossRef](#)]
35. Thangappan, R.; Kalaiselvam, S.; Elayaperumal, A.; Jayavel, R.; Arivanandhan, M.; Karthikeyan, R.; Hayakawa, Y. Graphene decorated with MoS₂ nanosheets: A synergetic energy storage composite electrode for supercapacitor applications. *Dalton Trans.* **2016**, *45*, 2637–2646. [[CrossRef](#)] [[PubMed](#)]

Disclaimer/Publisher's Note: The statements, opinions and data contained in all publications are solely those of the individual author(s) and contributor(s) and not of MDPI and/or the editor(s). MDPI and/or the editor(s) disclaim responsibility for any injury to people or property resulting from any ideas, methods, instructions or products referred to in the content.